14.4 Numerical simulation of a tornadogenesis in a mini-supercell associated with Typhoon Shanshan on 17 September 2006

Wataru Mashiko*, Hiroshi Niino**, and Teruyuki Kato*
*Meteorological Research Institute, Tsukuba, Japan
**Ocean Research Institute, University of Tokyo, Tokyo, Japan

1. Introduction

On 17 September 2006, three tornadoes occurred on the east coast of Kyusyu Island in western Japan during the passage of an outer rainband in the right-front quadrant of Typhoon Shanshan. In order to clarify the structure of the tornado-producing storms and the mechanism of tornadogenesis, we performed numerical simulations with high resolutions using a nonhydrostatic model.

2. Overview of synoptic and mesoscale fields based on observational data

Strong typhoon Shanshan with a central pressure of 950 hPa moved north-northeastward at a speed of 35 km h^{-1} over the East China Sea in the west of Kyusyu Island when three tornadoes hit Nichinan, Hyuuga and Nobeoka on the east coast in Kyusyu Island at about 1210, 1330 and 1410 Japan Standard Time (JST, JST = UTC + 9 hours) on 17 September 2006, respectively. The occurrence point of each tornado was located in the right-front quadrant of the moving typhoon. Radar image at 1400 JST shows that two adjacent rainbands extend from the north to the east side of the typhoon about 300 km away from the typhoon center (Fig. 1). All of the three tornadoes were generated during the passage of the outermost rainband, which consisted of a number of isolated convective systems with a horizontal scale of 20-40 km (Figs. 2a and 2b). Some of them lasted for more than 2 hours and spawned the tornadoes.

Corresponding author: Wataru Mashiko
Meteorological Research Institute, 1-1 Nagamine, Tsukuba, Ibaraki 305-0052, Japan
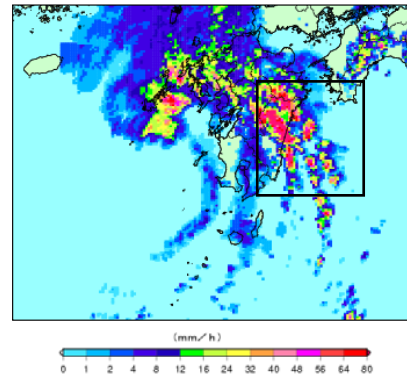E-mail: wmashiko@mri-jma.go.jp

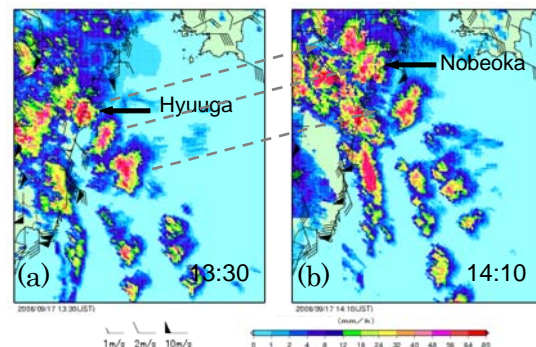Fig. 1. Precipitation intensity estimated from radar observation at 1400 JST.

Fig. 2. Same as Fig. 1, but for the rectangle framed area in Fig. 1 (a) at 1330 JST and (b) at 1410 JST.

3. Numerical model

The numerical model used in this study is the nonhydrostatic model (JMANHM; Saito et al. 2006) developed by Japan Meteorological Agency (JMA). To conduct high-resolution model integrations, quadruply one-way nested grids are used. Hereafter, the experiments with horizontal grid spacings of 5 km, 1 km, 250 m and 50 m are referred to as NHM5km, NHM1km, NHM250m and NHM50m, respectively. Figure 3a shows the model domains of NHM1km, NHM250m

and NHM50m. The vertical coordinate is terrain-following (z^*). Nesting procedures of the experiments are shown in Fig.3b. The initial and boundary conditions of NHM5km were provided from the operational regional analysis of JMA, which adopted a 4-dimensional variational data assimilation system. Unlike the previous numerical studies, the present simulations include complex real-topography and surface friction.
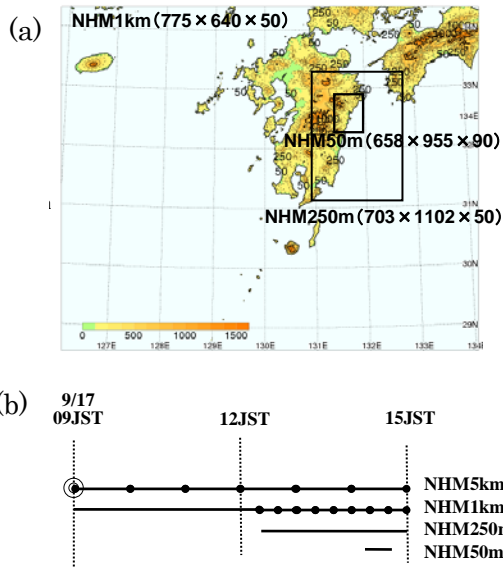
(a)

(b)

Fig. 3. (a) Model domains of NHM1km, NHM250m and NHM50m. Numerals show the number of grids on each direction ($x \times y \times z$). (b) Nesting procedures of the experiments.

4. Environmental field around the outermost rainband

NHM1km successfully reproduced two adjacent rainbands in the right-front quadrant of translating Shanshan (not shown). The simulated wind hodograph at Nobeoka location just prior to the passage of the simulated outermost rainband, which is assumed to correspond to the observed rainband consisting of the tornado-producing convective systems (Figs. 2a and 2b), shows that strong veering shear exists especially below 2-km height (Fig. 4). The strong veering shear having large helicity is distributed along the outermost rainband, especially in its eastern

(outer) side (not shown). Convective available potential energy (CAPE) around this rainband is about 1200 J Kg^{-1}, which is lower than about 2000 J Kg^{-1} in the southern area of (not shown). Therefore, the tornado environment is characterized by strong low-level veering shear and modest CAPE.
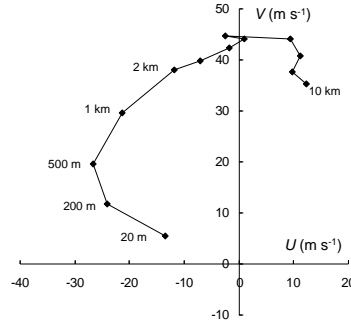

Fig. 4. Hodograph of simulated winds at Nobeoka at 1420 JST. Numerals next to profile indicate heights, and solid squares are plotted with an interval of 1 km above 1 km height.

5. Structure of a simulated mini-supercell

Figure 5 shows the simulated rainband by NHM250m at 1420 JST. The outermost rainband consists of a number of isolated convective systems with a horizontal scale of 20–40 km, which agrees with the radar observation (Figs. 2a and 2b). Several convective systems turn out to have characteristics similar to typical supercell storms: A hook-shaped pattern, found in the distribution of the mixing ratio of hydrometeors, exists at the southern tip of the convective system at a height of 1 km (Fig. 6a). The vertical cross section of hydrometeors, vertical velocity and vertical vorticity along the line A-B in Fig. 6a is shown in Fig. 6b. The strong updraft of more than 30 m s^{-1} forms a "vault" structure of the hydrometeors. Regions of large vertical vorticity overlap with those of a strong updraft: Maximum vertical vorticity exceeding 6×10^{-2} s^{-1} and updraft with larger than 30 m s^{-1} are found at about 1 km and 3 km height. The horizontal and vertical dimensions of the storm in the rainband are both only about 5 km, which are smaller than those of a classic supercell over the Great Plains in the United States. Thus, the simu-

lated storm is similar to a mini-supercell associated with a tropical cyclone (e.g., McCaul and Weisman 1996). Another feature to be noted is that the gust font near the surface boundary is distinguishable by the horizontal wind shear and large vertical vorticity, but is accompanied with a very small horizontal gradient of potential temperature.
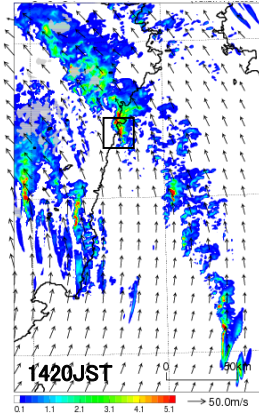

Fig. 5. Horizontal distribution of hydrometeors including rainwater, snow and graupel (g/kg) at a height of 1 km at 1420 JST simulated by NHM250m. Vectors denote ground-relative winds.
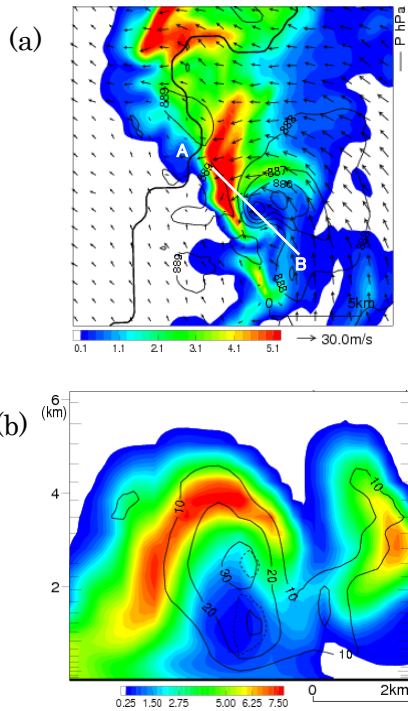

Fig. 6. (a) A close-up view of the rectangle area in Fig. 5. Arrows depict storm-relative wind vectors, and contour lines denote isobars with an interval of 1 hPa. (b) Vertical cross section along the line A-B in (a). Solid contour lines denote vertical velocity with an interval of 10 m s-1. Dashed line represents vertical vorticity contour of the 0.06 s-1.

6. Tornadogenesis in the mini-supercell simulated by NHM50m

a. Evolution of a low-level mesocyclone and a tornado

Figure 7 shows time series of minimum sea level pressure (SLP_{min}), maximum near-surface vertical vorticity at $z^* = 60$ m (VOR_{max}) and the horizontal distance between the location of VOR_{max} and the low-level mesocyclone center which is defined as the location of the maximum vertical vorticity over a 1-km square average at a height of 1 km. A rapid increase of VOR_{max} and sudden drop of SLP_{min} occurred just after 14:27:00 JST (hereafter, hh:mm:ss JST). The VOR_{max} reached 1.19 s^{-1} and the pressure drop about 14 hPa at the peak. In this study, we defined a tornado as a vortex having VOR_{max} larger than 0.65 s^{-1} conventionally. The distance between the VOR_{max} location and the low-level mesocyclone center is shown only during the tornado period in Fig. 7. The tornado was generated offshore and about 700 m away from the low-level mesocyclone center at 14:27:18 JST. The distance between VOR_{max} location and the low-level mesocyclone center increases with time, and the tornado dissipated after the landfall at 14:33:24 JST. The tornado lasted for about 6 minutes.
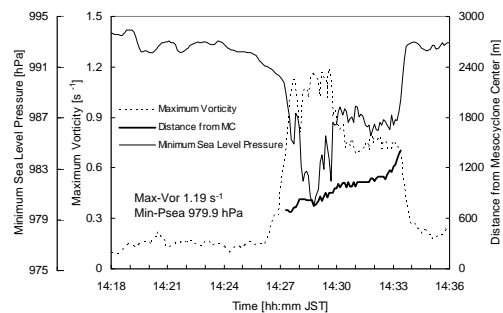

Fig. 7. Time series of minimum sea level pressure (SLP_{min}, solid line), maximum vertical vorticity at $z^* = 60$ m (VOR_{max}, dashed line), and the distance between the location of VOR_{max} and the low-level mesocyclone center (bold line) as simulated by NHM50m. The low-level mesocyclone center was determined as the location of maximum vertical vorticity on the 1-km square average at a height of 1 km. Each value was calculated within a 2.5 km radius of the low-level mesocyclone center. The distance is shown only for the period when the vortex satisfied the tornado criterion.

b. Tornado location in the mini-supercell and its structure

Figures 8a and 8b show the horizontal cross sections of the vertical velocity at a height of 150 m and the potential temperature at $z^* = 20$ m at 14:28:30 JST (72 sec after the tornadogeneis), respectively. At low levels, the simulated mini-supercell exhibits many features similar to the conceptual model of a tornadic supercell (e.g., Lemon and Doswell, 1979), in which the supercell has two main downdrafts called forward-flank downdraft (FFD) and rear-flank downdraft (RFD), and two surface fronts of forward-flank and rear-flank gust fronts. These two gust fronts are discernable by large vertical vorticity and wind shear with slight gradient of the potential temperature (about 1 K). The tornado is located on the rear-flank gust front near the mesocyclone center, which is close to the intersection point between the rear-flank and forward-flank gust fronts (Fig. 8b). Note that the tornado is located between the left-front edge of the RFD wrapping around the low-level mesocyclone and the strong updraft near the mesocyclone center (Fig. 8a). A close-up view of the rectangle area in Fig. 8a

is shown in Fig. 9a. A strong downdraft of more than 10 m s^{-1} exists in the eastern part of the tornado. It corresponds to the occlusion downdraft which is caused by a dynamically induced downward pressure gradient force associated with the strong low-level vorticity (Klemp and Rotunno 1983).

Now we briefly examine the structure of the simulated tornado, although the resolution in this simulation is too coarse to resolve it reliably. The diameter of the vortex near the surface is about 500 m, based on the outermost closed pressure contour line (Fig. 9a). The tornado exhibits a remarkable asymmetric structure with respect to both the vertical velocity and the horizontal wind speed. Horizontal wind exceeding 50 m s^{-1} exists only on the right side of the moving direction (Fig. 9a). Vertical cross section of the cloud water along the line A-B in Fig. 8a is shown in Fig. 9b. A funnel-shaped cloud which collocates with pressure deficit and large vertical vorticity is found. The tornado tilts north-westward with increasing height and connects to the low-level mesocyclone at a height of about 1 km.
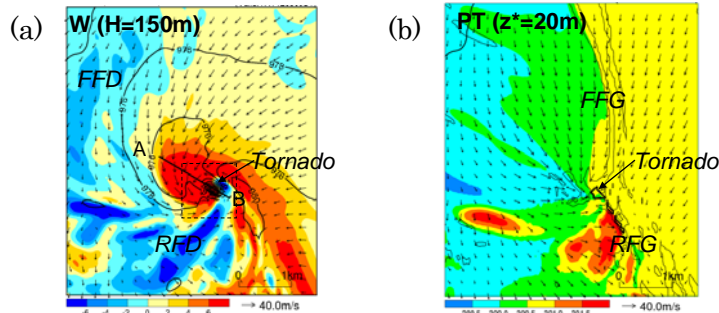

Fig. 8. (a) Horizontal cross section of vertical velocity at a height of 150 m at 14:28:30 JST. Contour lines denote pressure with an interval of 2 hPa. Arrows denote storm-relative wind vectors. (b) Horizontal cross section of potential temperature at $z^* = 20$ m. Thin and thick contour lines correspond to vertical vorticity of 0.01 s^{-1} and 0.10 s^{-1}, respectively. Arrows denote storm-relative wind vectors.
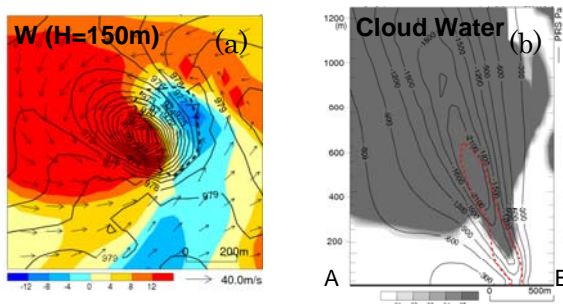

Fig. 9. (a) A close-up view of the tornado region in the rectangle area in Fig. 8a, but shaded tone is changed. Pressure contour lines are drawn for each 1 hPa. Heavy dashed contour line corresponds to ground-relative wind of 50 m s^{-1}. (d) Vertical cross section of cloud water along the line A-B in Fig.8a. Contour lines denote pressure perturbation with an interval of 300 Pa, and heavy dashed contour line corresponds to vertical vorticity of 0.50 s^{-1}.

c. Generation process of the tornado in the mini-supercell

The generation process of the simulated tornado is carefully examined here. Figures 10a-d show the horizontal distributions of hydrometeors, isobars and horizontal grid vectors at a height of 1 km with an interval of 30 sec from 14:26:00 to 14:27:30 JST (just after the tornadogenesis). At this level, the hydrometeors only consist of rain water. The distribution of the RFD (Figs. 10e-h) is collocated well with the hook-shaped hydrometeors (Figs. 10a-d), and propagates around the near-surface circulation center. The main updraft lays ahead and to the left of the RFD. The advancing RFD enhances the low-level convergence at its leading edge, making the updraft region in a horseshoe shape with time. A close-up view of the square area surrounded by the dashed line in Figs. 10e-h shows that two bands with strong updraft extend southward from the rotating main updraft near the mesocyclone center (Figs. 10i and 10j). The eastern updraft is associated with the rear-flank gust front, while the western updraft is located ahead of the advancing RFD. The outflow from the RFD enhanced the low-level convergence and resulted in the latter updraft. The leading edge of the RFD approaches the rear-flank gust front with time and eventually reached it (Figs. 10k and 10l). The most notable is that the tornado is generated at the region of a strong updraft near the mesocyclone center on the left-front edge of the RFD right after the RFD reaches the rear-flank gust front (Fig. 10l). Judging from the evolution of the RFD, the RFD instigates the tornadogenesis.

Figure 11b illustrates the backward trajectories of twenty-one parcels, which are distributed in the tornado region at a height of 150 m at 14:27:30 JST (Fig. 11a). The three-dimensional model outputs of 1-sec interval are used for the integration, where the Euler scheme with a time step of 0.5 sec is adopted. Note that the trajectory calculations were performed with storm-relative winds. The trajectory analysis reveals that about half of the parcels located in the tornado region at 17:27:30 JST originate from the RFD (Fig. 11b). These parcels descend cyclonically from the middle level (higher than 500 m for several parcels) to near the surface through the RFD and then ascend into the vortex center sharply.
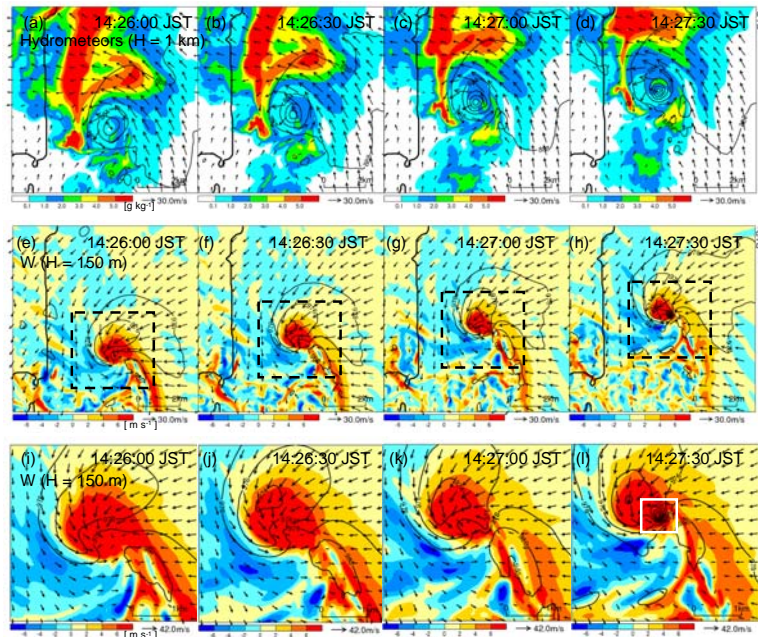

Fig. 10. Evolution of (a)-(d) hydrometeors (rainwater, snow and graupel) at a height of 1 km, and (e)-(h) vertical velocity at a height of 150 m from 14:26:00 to 14:27:30 JST with an interval of 30 sec until the tornado genesis. (i)-(l) A close-up view of the rectangle area in (e)-(h). Contour lines indicate pressure with an interval of 2 hPa, and arrows denote storm-relative wind vectors.
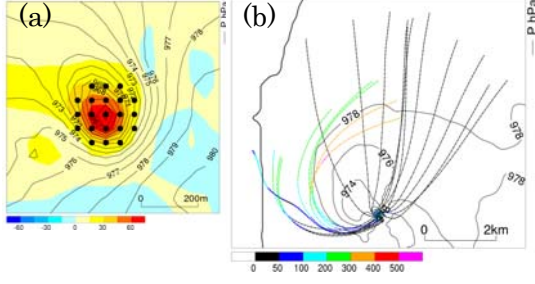
Fig. 11. (a) Initial locations of parcels for backward trajectory analysis at 14:27:30 JST. The displayed areas are shown by the solid frames in Fig. 10l. All parcels are disposed at a height of 150 m. Shaded color represents vertical vorticity. Contour lines indicate pressure with an interval of 1 hPa. (b) Projection of the three-dimensional backward trajectories. Parcels were integrated backward for 270 sec. Colors indicate the parcel heights. Contour lines denote pressure with an interval of 1 hPa at 14:27:30 JST.

d. Vorticity budget analysis along the trajectory through the RFD

In order to clarify the mechanism for the tornadogenesis, the source and amplifying process of the vertical vorticity in the tornado must be identified. Studied in this subsection is the budget analysis for the vertical and horizontal components of vorticity along the trajectory traveling through the RFD. The equation for vertical vorticity (ζ) is given by

$$\frac{D\zeta}{Dt} = -\zeta\left(\frac{\partial u}{\partial x}+\frac{\partial v}{\partial y}\right)-\left(\frac{\partial w}{\partial x}\frac{\partial v}{\partial z}-\frac{\partial w}{\partial y}\frac{\partial u}{\partial z}\right)+\frac{1}{\rho^2}\left(\frac{\partial \rho}{\partial x}\frac{\partial p}{\partial y}-\frac{\partial \rho}{\partial y}\frac{\partial p}{\partial x}\right)+\frac{1}{\rho}\left(\frac{\partial F_y}{\partial x}-\frac{\partial F_x}{\partial y}\right) \quad (1)$$

where u, v, and w are the three-dimensional velocity components, ρ is the density, p is the pressure, F_x and F_y are the x and y components of turbulent mixing. The terms on the right-hand side represent horizontal convergence of vertical vorticity, tilting of horizontal vorticity into the vertical, solenoidal term, and frictional term, respectively. Coriolis force is neglected.

Figure 12a shows a representative path of a parcel that is located at a height of 150 m near the center of the tornado at 14:27:30 JST (just after tornadogenesis) and originates from the RFD. Figure 12b displays the time sequence of the vertical vorticity, parcel height and terms in Eq. (1) during the final 90 sec of the trajectory shown in Fig. 12a. Note that the solenoidal term is not shown since it is always less than the order of 10^{-4} s^{-1}. The parcel first descends while having a small negative vertical vorticity. After that, the vertical vorticity increases and changes its sign before the parcel reaches its nadir at 14:27:09 JST. Throughout most of its descent, both the tilting term and the convergence term have considerably small magnitude. However, the tilting term increases rapidly right before the parcel reaches the lowest part of its trajectory, and the vertical vorticity has a positive value of about 0.01 s^{-1}. Once the trajectory turns upward, the convergence term becomes dominant, resulting in a rapid increase of vertical vorticity. The frictional effect works negatively after the vertical vorticity intensifies.

We also need to examine the evolution of the horizontal vorticity, which is tilted into the vertical and eventually amplified by the horizontal convergence. To this end, it is convenient to write down the equations in seminatural coordinates, where (s, n, k) represent orthonormal basis vectors with the wind vector V = (V_h, 0, w) (e.g., Adlerman et al. 1999). The equations for the streamwise and crosswise horizontal vorticities, ω_s and ω_n, respectively, are

$$\frac{D\omega_s}{Dt} = \omega\frac{D\psi}{Dt}-\omega(V_h\frac{\partial\psi}{\partial n}+\frac{\partial w}{\partial z})-(\frac{\partial V_h}{\partial n}\frac{\partial w}{\partial s}-V_h\frac{\partial V_h}{\partial z}\frac{\partial\psi}{\partial s})+\frac{1}{\rho^2}(\frac{\partial\rho}{\partial n}\frac{\partial p}{\partial z}-\frac{\partial\rho}{\partial z}\frac{\partial p}{\partial n})+\frac{1}{\rho}(\frac{\partial F_z}{\partial n}-\frac{\partial F_n}{\partial z}) \quad (2)$$

$$\frac{D\omega_n}{Dt} = -\omega\frac{D\psi}{Dt}-\omega(\frac{\partial V_h}{\partial s}+\frac{\partial w}{\partial z})-(V_h\frac{\partial\psi}{\partial z}\frac{\partial V_h}{\partial n}-V_h\frac{\partial\psi}{\partial s}\frac{\partial w}{\partial n})+\frac{1}{\rho^2}(\frac{\partial\rho}{\partial z}\frac{\partial p}{\partial s}-\frac{\partial\rho}{\partial s}\frac{\partial p}{\partial z})+\frac{1}{\rho}(\frac{\partial F_s}{\partial z}-\frac{\partial F_z}{\partial s}) \quad (3)$$

where $\Psi = \tan^{-1}(v/u)$ is the horizontal angle of horizontal velocity vector that increases counterclockwise from the east. The first term on the rhs of both equations represents an exchange between steramwise and crosswise vorticity due to change in the direction of the horizontal velocity. The second and third terms in the rhs of each equation represent the rate of change of streamwise/crosswise vorticity from the convergence (horizontal stretching) and tilting of

vortex tubes, respectively. Solenoidal term and frictional term are represented by the fourth and fifth terms in the rhs, respectively.

Figures 12c and 12d display time evolution of horizontal vorticity components and the terms in Eqs. (2) and (3) along the same trajectory for 330 sec until just after the tornadogenesis (14:27:30 JST). The streamwise vorticity is the dominant component of three-dimensional vorticity and increases steadily until the parcel reaches the lowest part of its trajectory, while the crosswise vorticity increased less rapidly. Note that the parcel originally has a remarkably large streamwise vorticity of about 0.04 s^{-1} at 14:22:00 JST and it was increased to 0.21 s^{-1} near its nadir.

Figure 12c clearly shows that the large increase in the streamwise vorticity results mainly from the convergence term throughout its descent, followed by the exchange and tilting terms. The frictional term is always negative and works effectively at the lower level (not shown). Note that the baroclinic generation term (solenoidal term) is less than the order of 10^{-4} s^{-1} and is small compared to other dominant terms. The tilting and convergence terms in the streamwise vorticity equation rapidly decrease and become negative right before the parcel reaches the lowest trajectory location, resulting in a rapid decrease of the streamwise vorticity. At the same time the streamwise vorticity is tilted into the vertical.
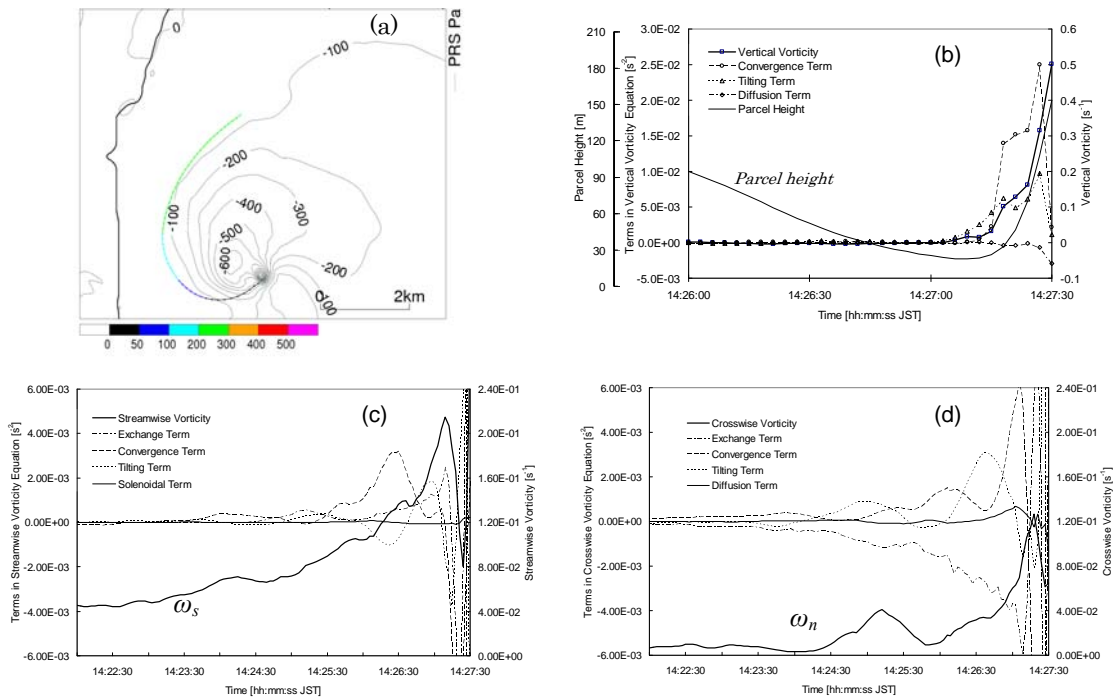

Fig. 12. Budget analysis of vorticity equation along the trajectory traveling through the RFD. (a) Projection of the 330-sec backward trajectory for the targeted parcel which is located near the tornado center at 14:27:30 JST. Plotted markers represent the parcel heights with an interval of 30 sec. (b) Time series of the terms in the vertical vorticity equation for the last 90-sec trajectory. Parcel height is also shown. (c) Time series of the terms in the streamwise vorticity equation. (d) Time series of the terms in the crosswise vorticity equation. The vorticity components (ζ, ω_s, ω_n) are also shown in each figure. The solenoidal terms in the vertical and crosswise directions and the frictional term in streamwise direction are omitted since they are relatively small compared to other terms.

In the crosswise direction, no single forcing term is dominant, but most of the crosswise horizontal vorticity is generated by the convergence and tilting terms. The exchange term tends to reduce the crosswise vorticity effectively with time. The solenoidal term is quite small (not shown). The frictional term does not give a significant contribution to the crosswise vorticity although it increases around the lowest part of the trajectory.

The analysis revealed that most of the streamwise vorticity that is tilted and stretched into the vertical arises principally from the amplification of the initial large streamwise vorticity (about 0.04 s^{-1}) due to the convergence term, followed by the exchange and tilting terms. Thus, our next concern is what the initial streamwise horizontal vorticity around 14:22:00 JST is. Most parcels traveling through the RFD cyclonically around the mesocyclone originate from the northern side of the mini-supercell between 200 and 500 m height. The wind hodograph in Fig. 4 represents the storm environment which has large horizontal vorticity vector directed west-southwestward between these levels. It is apparent that the large streamwise vorticity of the parcels originates in the storm environment with strong low-level vertical wind shear.

The RFD is important for the tornadogenesis because it transports parcels with significant streamwise horizontal vorticity associated with the environmental vertical shear barotropically to low levels. In addition, when the RFD associated with the hook-shaped precipitation pattern hits the rear-flank gust front it causes locally intensified surface convergence on the left-front edge of the RFD, which amplifies vertically tilted streamwise vorticity significantly.

e. What causes the RFD to wrap around the mesocyclone cyclonically?

To clarify what caused the RFD to wrap around the mesocyclone cyclonically, which is a key role in the tornadogenesis, we have calculated each term in the vertical momentum equation diagnostically. The equation of a Lagrangian time rate of change is, to the approximation,

$$\frac{Dw}{Dt} = -\frac{1}{\rho}\frac{\partial p'}{\partial z} - \frac{1}{\rho}\rho'g \qquad (4)$$

where p' is the pressure perturbation, ρ' the density fluctuation from the basic state of $\bar{\rho}$, and g the gravity acceleration.

Horizontal plots of the terms in Eq. (4) at a height of 250 m at 14:26:00 JST are shown in Figs. 13a-c. Figure 13a shows that the perturbation pressure gradient forcing is strongly positive near the mesocyclone circulation center. In the surrounding region around the mesocyclone, the perturbation pressure gradient forcing is slightly positive. However, a strong negative forcing exists in a small area to the west of the mesocyclone. In the meanwhile, a region of negative buoyancy spreads from the northwest to the south of the mesocyclone. This region is collocated with the RFD (cf., Fig. 13b and Fig. 10a). The negative buoyancy in the northwest quadrant of the low-level mesocyclone contributes significantly to the downward acceleration of the vertical velocity (Fig. 13c), which causes the trajectories in the RFD to start descending and accelerate further downward.

In order to identify the contribution of precipitation loading to the buoyancy, the buoyancy term in Eq. (4) was decomposed. Figures 14a and 14b show the horizontal distribution of the buoyancy due to the precipitation loading and the other contribution, respectively. The distributions of the two contributions to the buoyancy exhibit quite similar pattern to each other (cf., Fig. 14a and Fig. 14b), and the negative buoyancy around the mesocyclone is nearly collocated with the RFD (cf., Fig. 14 and Fig. 10e) and the hook-shaped hydrometeors (cf., Fig. 14 and Fig. 10a). However, the negative buoyancy caused by the precipitation loading contributes more effectively, especially in the northwest quadrant around the mesocyclone. Thus, instead of the evaporative cooling, the precipitation loading is the determining factor for the formation of the RFD to wrap around the mesocyclone cyclonically.
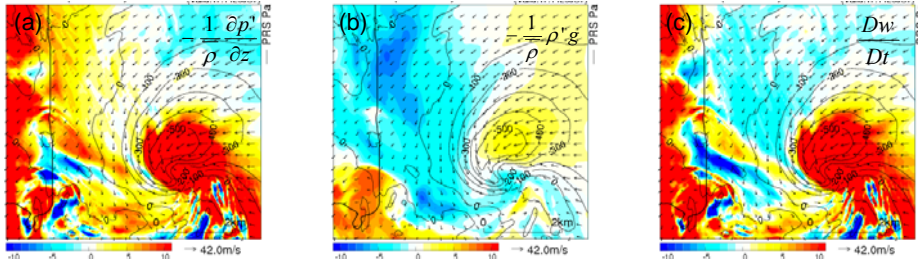
Fig. 13. Horizontal cross section of (a) perturbation pressure gradient forcing, (b) buoyancy forcing and (c) acceleration term which is sum of (a) and (b) in the vertical momentum equation at a height of 250 m at 14:26:00 JST. The pressure contour lines are drawn for each 1 hPa. Arrows denote storm-relative wind vectors.
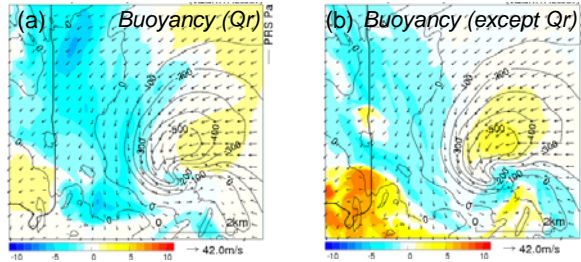

Fig. 14. Horizontal cross section of (a) buoyancy due to the precipitation loading, and (b) buoyancy due to the other contributions at a height of 150 m at 14:26:00 JST. The contour lines of pressure are drawn for each 1 hPa. Vectors denote storm-relative winds.

7. Sensitivity experiment

In order to examine the effect of precipitation loading on the RFD and the subsequent tornadogenesis, we have performed sensitivity experiment "NOLOAD" in which the weight of the precipitation (rain, snow and graupel) is neglected in the density in the governing equations of the model simulation.

The simulation result shows a remarkable difference from the control run. A much weaker tornado (maximum $VOR_{max} = 0.68$ s^{-1} and minimum $SLP_{min} = 987.9$ hPa), which barely satisfies the tornado criteria of this study, is generated about 4 min later compared to the control run and dissipates quickly (Fig. 15). The remarkable difference is seen in the behavior of the RFD. The RFD does not wrap around the low-level mesocyclone cyclonically and exists only in the southwestern portion of the mesocyclone unlike the control run (Fig. 16). The sensitivity experiment indicates that the tornadogenesis is extremely sensitive to the behavior of the RFD. The precipitation loading associated with hook-shaped hydrometeors plays a key role in the behavior of the RFD and the subsequent tornadogenesis.
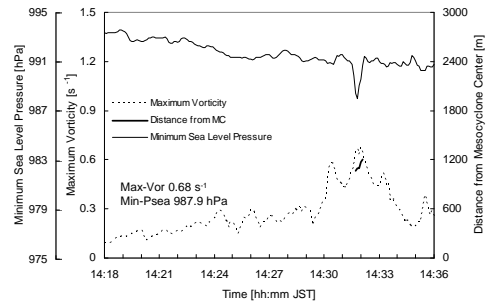

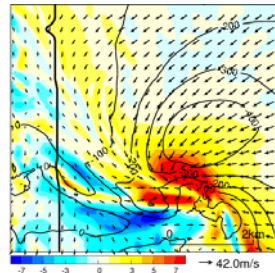Fig. 15. Same as Fig. 7 except for the experiment without precipitation loading (NOLOAD).

Fig. 16. Same as in Fig. 10e except for the experiment without precipitation loading (NOLOAD).

8. Summary

At least three tornadoes hit the east coast of Kyusyu Island in western Japan during the passage of an outermost rainband in the right-front quadrant of Typhoon Shanshan on 17 September 2006.

The simulation well reproduced the outermost rainband on the right-front quadrant of the typhoon. The environment around the rainband was characterized by strong low-level veering shear and modest CAPE of about 1200 J Kg^{-1}. The rainband consisted of a number of isolated convective systems with a horizontal scale of 20-40 km. Some of the systems contained a hook-shaped pattern and vault-like structure of hydrometeors at their southern edge. They had a strong rotating updraft of more than 30 m s^{-1} with vertical vorticity exceeding 0.06 s^{-1}. The horizontal and vertical dimensions of the storms were both only about 5 km, and a near-surface temperature difference across the gust front was very small (about 1 K). These characteristics clearly show that the storms were mini-supercells.

The innermost simulation with a horizontal grid spacing of 50 m successfully reproduced a tornado spawned by the mini-supercell approaching the coast of Nobeoka. The diameter of the tornado in pressure field near the surface was about 500 m, and the vertical vorticity exceeded 1.0 s^{-1}. The tornado was generated on the rear-flank gust front near the mesocyclone center when the left-front edge of the RFD, which was wrapping around the low-level mesocyclone, reached the rear-flank gust front.

We conclude that the RFD, which wraps around the mesocyclone cyclonically, plays a key role in the tornadogenesis by barotropically transporting large streamwise horizontal vorticity associated with low-level vertical shear in the environment toward the surface. Moreover, the leading-edge of the RFD enhances the horizontal convergence, especially at the left-front edge of the RFD, when the RFD reaches the rear-flank gust front. The horizontal convergence rapidly amplifies vertical vorticity tilted from streamwise vorticity and forms a tornado. The behavior of the RFD is largely affected by the negative buoyancy due to the precipitation loading. The precipitation loading in the area of hook-shaped precipitation pattern is crucial to the formation of the RFD to wrap around the mesocyclone and the subsequent tornadogenesis.

REFERENCES

Adlerman, E. J., and K. K. Droegemeier, 1999: A numerical simulation of cyclic mesocyclogenesis. J. Atmos. Sci., 56, 2045-2069.

Klemp, J. and R. Rotunno, 1983: A study of the tornadic region within a supercell thunderstorm. J. Atmos. Sci., 40, 359-377.

Lemon, L. R., and C. A. Doswell III, 1979: Severe thunderstorm evolution and mesocyclone structure as related to tornadogenesis, Mon. Wea. Rev., 107, 1184-1197.

McCaul, E. W., Jr., and M. L. Weisman, 1996: Simulation of shallow supercell storms in landfalling Hurricane environments. Mon. Wea. Rev., 124, 408-429.

Saito, K., T. Fujita, Y. Yamada, J. Ishida, Y. Kumagai, K. Aranami, S. Ohmori, R. Nagasawa, S. Kumagai, C. Muroi, T. Kato, H.Eito, and Y. Yamazaki, 2006: The operational JMA nonhydrostatic mesoscale model. Mon. Wea. Rev., 134, 1266-1298.